



Protoplanetary Disks around Sun-like Stars Appear to Live Longer When the Metallicity is Low*

Guido De Marchi¹, Giovanna Giardino², Katia Biazzo³, Nino Panagia⁴, Elena Sabbi^{4,5}, Tracy L. Beck⁴, Massimo Robberto⁴, Peter Zeidler⁶, Olivia C. Jones⁷, Margaret Meixner^{8,9}, Katja Fahrion¹, Nolan Habel^{8,9}, Conor Nally¹⁰, Alec S. Hirschauer⁴, David R. Soderblom⁴, Omnarayani Nayak¹¹, Laura Lenkie^{8,9}, Ciaran Rogers¹², Bernhard Brandl¹², and Charles D. Keyes⁴

¹ European Space Research and Technology Centre, Keplerlaan 1, 2200 AG Noordwijk, Netherlands; gdemarchi@esa.int

² ATG Europe for the European Space Agency, European Space Research and Technology Centre, Noordwijk, Netherlands

³ INAF Osservatorio Astronomico di Roma, Via Frascati 33, 00078 Monteporzio Catone, Rome, Italy

⁴ Space Telescope Science Institute, 3700 San Martin Drive, Baltimore, MD 21218, USA

⁵ Gemini Observatory/NSF NOIRLab, 950 North Cherry Avenue, Tucson, AZ, 85719, USA

⁶ AURA for the European Space Agency, ESA Office, STScI, 3700 San Martin Drive, Baltimore, MD 21218, USA

⁷ UK Astronomy Technology Centre, Royal Observatory, Blackford Hill, Edinburgh, EH9 3HJ, UK

⁸ Jet Propulsion Laboratory, California Institute of Technology, 4800 Oak Grove Drive, Pasadena, CA 91109, USA

⁹ SOFIA Science Center, USRA, NASA Ames Research Center, M.S. N232-12, Moffett Field, CA 94035, USA

¹⁰ Institute for Astronomy, University of Edinburgh, Blackford Hill, Edinburgh, EH9 3HJ, UK

¹¹ Goddard Space Flight Center, 8800 Greenbelt Road, Greenbelt, MD 20771, USA

¹² Leiden Observatory, Leiden University, Leiden, The Netherlands

Received 2023 December 4; revised 2024 September 1; accepted 2024 September 3; published 2024 December 16

Abstract

Previous Hubble Space Telescope observations of the star-forming cluster NGC 346 in the Small Magellanic Cloud (SMC) revealed a large population of pre-main-sequence (PMS) candidates, characterized by $H\alpha$ excess emission in their photometry. However, without access to spectroscopy, the nature of these objects remained unclear. Using the NIRSpec instrument on board JWST, we studied a sample of these stars, with masses in the range of $\sim 0.9\text{--}1.8 M_{\odot}$, effective temperatures (T_{eff}) in the range of 4500–8000 K, and PMS ages between ~ 0.1 and 30 Myr. Here, we present the first spectra of solar-mass PMS stars in the metal-poor SMC ($Z = 1/8 Z_{\odot}$) and discuss the physical properties of 10 representative sources with good signal-to-noise ratio. The observations indicate that even the oldest of these PMS candidates are still accreting gas with typical rates of $\sim 10^{-8} M_{\odot} \text{ yr}^{-1}$ for stars older than ~ 10 Myr, confirming their PMS nature. The spectra also reveal near-infrared excess and molecular hydrogen excitation lines consistent with the presence of disks around these stars. These findings suggest that in a low-metallicity environment, circumstellar disks can live longer than previously thought.

Unified Astronomy Thesaurus concepts: Star formation (1569); Pre-main sequence stars (1290); Stellar accretion (1578); Young star clusters (1833); Small Magellanic Cloud (1468); Spectroscopy (1558)

1. Introduction

In their final formation stages, after dissipating most of the envelope of dust and gas in which they were born, Sun-like stars still have a mostly gaseous disk from which they continue to accrete while the star contracts until hydrogen ignites in the core (C. Hayashi 1966; F. H. Shu et al. 1987; F. Palla & S. W. Stahler 1999; R. B. Larson 2003). It is in these disks that planetary systems form (P. J. Armitage 2010). In nearby Galactic star-forming regions with solar composition, the disks are short-lived, with decay timescales of ~ 2 Myr and an accretion phase that rapidly tapers off (K. E. Haisch et al. 2001; J. Hernandez et al. 2008; E. E. Mamajek 2009; D. Fedele et al. 2010; A. J. W. Richert et al. 2018).

Since the majority of stars in the Universe formed at cosmic noon around redshift $z \sim 2$ (P. Madau et al. 1996; S. Lilly et al. 1996), it is important to investigate the lifetime of protoplanetary

disks in the lower-metallicity conditions ($Z \sim 0.1 Z_{\odot}$) characteristic of those environments (e.g., M. Zwaan et al. 2005; J. Fynbo et al. 2006). In this respect, it has been suggested that lifetimes in lower-metallicity environments should be even shorter than in the solar neighborhood because disks are less shielded by dust from the X-ray emission of the central star (B. Ercolano et al. 2008, 2009). The fraction of disk-bearing stars with near-infrared (NIR) excess measured in two small low-metallicity ($\sim 0.1 Z_{\odot}$) star-forming regions in the extreme outer Galaxy initially (C. Yasui et al. 2009, 2010) appeared to support this hypothesis (but see Section 6).

In contrast, photometric studies of equally low-metallicity star-forming regions in the Magellanic Clouds using the Hubble Space Telescope (HST) have revealed thousands of stars that appear to systematically accrete at higher rates and for times exceeding 30 Myr (G. De Marchi et al. 2010, 2011a, 2013, 2017; K. Biazzo et al. 2019; S. Tsilia et al. 2023). In particular, observations (E. Sabbi et al. 2007) of the massive star-forming region NGC 346, in the Small Magellanic Cloud (SMC), revealed approximately ~ 690 objects with strong $H\alpha$ excess emission and $H\alpha$ equivalent widths (EWs) larger than 20 \AA (G. De Marchi et al. 2011a). As such, these objects are candidate pre-main-sequence (PMS) stars actively accreting matter from their circumstellar disks. G. De Marchi et al. (2011a) find

* Based on observations made with the NASA/ESA/CSA James Webb Space Telescope.



Original content from this work may be used under the terms of the [Creative Commons Attribution 4.0 licence](https://creativecommons.org/licenses/by/4.0/). Any further distribution of this work must maintain attribution to the author(s) and the title of the work, journal citation and DOI.

that these PMS objects form two distinct populations, with a clearly bimodal age distribution: about half of the objects are younger than ~ 2 Myr and the other half older than ~ 8 Myr, including over 200 objects with ages in the range of 15–30 Myr (see Section 5 for details).

Since in Galactic star-forming regions accreting PMS stars older than 15 Myr are very rare (G. J. Herczeg & L. A. Hillenbrand 2014), it has been proposed (G. De Marchi et al. 2010, 2011a, 2013, 2017) that the PMS accretion phase lasts longer in the low-metallicity environments typical for the Magellanic Clouds (~ 0.1 – $0.3 Z_{\odot}$), and by inference at cosmic noon. While other processes, such as chromospheric activity or binary interactions, might be responsible for the $H\alpha$ excess emission in HST photometry of stars hotter than ~ 7500 K, this is unlikely because the measured $H\alpha$ emission EW is more than an order of magnitude higher than for chromospherically active binaries (D. Montes et al. 1995). However, without a means to obtain spectra for these objects, the nature of the $H\alpha$ excess emission of the sources in NGC 346 has so far remained unclear.

With the NIRSpec Micro Shutter Array (MSA), we studied a sample of these candidate PMS objects in NGC 346, as well as normal main-sequence (MS) stars with no detectable $H\alpha$ excess emission. Here, we present the spectra and discuss the physical properties of 10 representative sources with similar masses (~ 0.9 – $1.8 M_{\odot}$), T_{eff} in the range of 4500–8000 K, and spanning a range of ages (~ 0.1 –30 Myr).

The structure of this paper is as follows. The observations are presented in Section 2, while the extraction and calibration of the spectra are discussed in Section 3. The spectral analysis is contained in Section 4, where we derive the physical parameters of the objects. A detailed discussion of the age of PMS stars and their uncertainties is provided in Section 5. Conclusions are presented in Section 6.

2. Observations and Sample Selection

The central regions of NGC 346 were observed with NIRSpec on 2022 July 26 using the G235M/F170LP medium-resolution grating ($R \sim 1000$) covering the range of 1.7– $3.2 \mu\text{m}$ (proposal number 1227). A total of 40 sources were observed simultaneously through the NIRSpec MSA, of which half had been identified as candidate PMS stars (G. De Marchi et al. 2011a), owing to their $H\alpha$ excess emission, and the other half as candidate MS stars (no detectable excess in $H\alpha$). The targets were selected from a catalog of about 80,000 sources in this field detected and measured with HST photometry (E. Sabbi et al. 2007), out of which about 690 have $H\alpha$ excess emission exceeding 5σ (G. De Marchi et al. 2011a).

Using the eMPT software tool (N. Bonaventura et al. 2023), we identified the most suitable targets (and corresponding MSA configuration) for the specific orientation of the telescope at the time of the observations. The MSA contains about 250,000 microshutters, each one defining a slit with a width of $0''.20$ and a length of $0''.46$, while the pitch between the microshutters is $0''.27$ in the spectral direction and $0''.53$ in the spatial direction (P. Ferruit et al. 2022). We elected to reserve for each source a “slitlet” composed of three neighboring microshutters in the cross-dispersion direction, in order to also properly characterize the nebular background around our targets. Each slitlet spans a region of $0''.2 \times 1''.5$ on the sky. Several constraints were applied to derive the final list of 40 targets, one of which was to

avoid sources with contaminants within three microshutters for any position of the source in the slitlet. Indicating with m_I the I -band magnitude of the possible target source in the catalog by E. Sabbi et al. (2007), we considered as viable targets only those for which any contaminants within the three microshutters were fainter than $m_I + 5$. We further constrained the eMPT tool to exclude objects for which the wavelengths corresponding to the $\text{Pa}\alpha$ or $\text{Br}\beta$ spectral lines would fall in the gap between detectors to ensure that both lines can be measured simultaneously. For some sources, the wavelength range around the $\text{Br}\gamma$ line is also recorded.

Each source was observed at three different nodding positions in the slitlet by slewing the telescope in the cross-dispersion direction by an amount corresponding to the microshutter pitch ($0''.53$). Each target star was observed for 481 s in each of the three microshutters, at the same relative position, for a total 1443 s of integration. Due to the fixed MSA pattern, it is not possible to locate all targets at the nominal center of a microshutter.

In this first work, we present the results for 10 representative sources with similar masses (0.9 – $1.8 M_{\odot}$, median $1.2 M_{\odot}$) that span a range of ages, including both younger and older PMS candidate stars, as well as MS objects. The stars were selected to have a signal-to-noise ratio (SNR) > 3 (as measured per pixel with the *DER_SNR* routine; F. Stoehr et al. 2008), to be free from contaminants in the immediate vicinity of the selected microshutters (some of the contaminants were not detectable in the optical HST images but are visible in the NIRCам exposures; O. C. Jones et al. 2023; N. Habel et al. 2024), and for which also the $\text{Br}\gamma$ is recorded in the spectrum (only for one of the objects this is not the case). In Table 1, we list the coordinates and key stellar parameters. The masses and ages of the PMS candidates were determined by G. De Marchi et al. (2011a) by comparing the effective temperature T_{eff} and bolometric luminosity L_{bol} of the stars, derived from extinction-corrected V and I broadband HST photometry, to theoretical PMS evolutionary tracks (S. Degl’Innocenti et al. 2008; E. Tognelli et al. 2011) for metallicity $Z = 1/8 Z_{\odot}$, as appropriate for NGC 346 (for more details, see G. De Marchi et al. 2011a and Section 5). For candidate MS stars, which were selected among objects with no $H\alpha$ excess emission in the catalog of G. De Marchi et al. (2011a), the masses were derived in the same way, by comparing the T_{eff} and L_{bol} of the stars to MS isochrones from the same set of models, after reddening correction. (Note that older PMS candidates and MS stars generally share the same position in the color–magnitude diagram (CMD), the only difference being the presence or absence of $H\alpha$ excess emission with $\text{EW} > 20 \text{ \AA}$.) The resulting masses are in the range of ~ 1.2 – $1.3 M_{\odot}$, comparable with those of the PMS candidates.

3. Spectral Extraction and Flux Calibration

The exposures were processed with the NIRSpec ramp-to-slope pipeline, developed by the ESA NIRSpec Science Operations Team (SOT), which performs the following basic data reduction steps: bias subtraction, reference pixel subtraction, linearity correction, dark subtraction, and finally count-rate estimation, including jump detection and cosmic-ray rejection (S. M. Birkmann et al. 2022). From the count-rate images, the flux- and wavelength-calibrated spectra were obtained using Stage 2 of the SOT NIRSpec Instrument Pipeline Software (NIPS; C. Alves de Oliveira et al. 2018b) to

Table 1
Properties of the Stars in Our Sample

ID	R.A.	Decl.	Age (Myr)	M_* (M_\odot)	A_V (mag)	$\log T$ (K)	$\log L$ (L_\odot)	R_* (R_\odot)	m_{200} (mag)	$W_{\text{Pa}\alpha}$ (Å)	$W_{\text{Br}\beta}$ (Å)	$W_{\text{Br}\gamma}$ (Å)	$\log L_a^{\text{H}\alpha}$ (L_\odot)	$\log L_a^{\text{Br}\gamma}$ (L_\odot)	$\log \dot{M}$ ($M_\odot \text{ yr}^{-1}$)
9884	14.8247272	−72.1544850	0.1	0.9	0.55	3.65	1.10	5.8	20.4	−142.1	−41.8	−21.5	1.02	1.28	−5.30
9685	14.8206427	−72.1862390	1.5	1.8	0.60	3.74	0.96	3.3	21.6	−65.1	−27.1	−10.6	0.25	0.39	−6.74
24897	14.8067222	−72.1913565	5.5	1.2	0.65	3.75	0.42	1.7	23.2	−210.0	−302.0	−25.8	−0.09	−0.27	−7.51
12559	14.8044053	−72.1929698	12.5	1.3	0.66	3.91	0.76	1.3	23.3	−157.8	−389.3	−8.0	−0.27	−0.99	−8.38
20408	14.7178504	−72.1690186	16.0	1.2	0.56	3.89	0.47	1.0	24.0	−165.2	−139.6	...	−0.32
26651	14.8120579	−72.1876153	20.0	1.0	0.60	3.82	0.31	1.1	23.9	−195.0	−129.7	−7.6	−0.59	−1.41	−8.76
40571	14.8088971	−72.1823255	27.0	0.9	0.55	3.80	0.03	0.8	24.4	−387.4	−290.0	−45.4	−0.10	−0.41	−7.68
10147	14.8854390	−72.1667293	...	1.3	0.56	3.89	0.86	1.5	23.1
14090	14.8811044	−72.1616790	...	1.4	0.55	3.88	0.68	1.3	23.4
19639	14.8660216	−72.1617760	...	1.2	0.42	3.84	0.45	1.2	23.9

Note. The columns correspond to the source identification (ID), J2000.0 coordinates (R.A., decl.), age, stellar mass (M_*), extinction (A_V), effective temperature ($\log T$), bolometric luminosity ($\log L$), stellar radius (R_*), magnitude in the F200W NIRCcam band (m_{200}), EW of the Pa α , Br β , and Br γ lines, accretion luminosity derived from the $L(\text{H}\alpha)$ and $L(\text{Br}\gamma)$ luminosity, and mass accretion rate ($\log \dot{M}$). Stellar parameters are from G. De Marchi et al. (2011a), NIRCcam F200W AB magnitudes are from N. Habel et al. (2024; F277W AB magnitudes for stars 9685 and 40571). All spectral lines have negative EW, indicating emission.

perform the following default operations (C. Alves de Oliveira et al. 2018a): subtract background, extract subimage containing the spectral trace, assign wavelength and spatial coordinates to each pixel therein, flat-fielding, and finally flux calibration. This procedure generates a rectified spectrum resampled on a regular two-dimensional (2D) grid, which in the case of our filter and grating combination (F170LP/G235M), produces images that span 7×1414 pixel², covering the wavelength range of $1.66\text{--}3.16\ \mu\text{m}$, and $0''.46$ in the cross-dispersion direction. The 2D-rectified spectra of two of our sources are shown in Figure 1.

To optimize the SNR, we computed the one-dimensional (1D) spectrum of each star from the 2D-rectified product by coadding three pixel rows around the nominal source position, as given by the MSA planning tool. To account for any slit losses and to perform absolute calibration, we rescaled each spectrum in order to match the corresponding magnitude of each source in the F200W band as observed with NIRCcam (N. Habel et al. 2024). The scale factor was derived by folding each observed spectrum through the NIRCcam F200W band using the *stsynphot* tool (STScI Development Team 2020) and comparing the resulting synthetic magnitude with the one actually observed. For stars 9685 and 40571, the magnitude in the F277W band was used instead since these objects were not observed with the F200W filter. The NIRCcam magnitudes are listed in Table 1.

Given the highly variable nebulosity in the region, background subtraction is a critical step. We take as a reference the two strong He I lines at $1.87\ \mu\text{m}$ and $2.06\ \mu\text{m}$, which are fully nebular in nature (the mass and T_{eff} of our targets are such that these lines are not expected to originate in their photospheres). We measure the flux of the He I lines by integrating over their width, after subtraction of the continuum. This is done for the spectrum containing source+background and for the two background spectra sampled by the microshutters just above and below the source. We take as a template of the nebular background the spectrum from the microshutter where the integrated He I line flux is closest to that in the spectrum with the source. We then rescale the background template (by multiplication) until the integrated He I line flux agrees with that in the spectrum of the source, and finally subtract the rescaled template from the spectrum of the source. The multiplicative factor is always smaller than 1.2 (i.e., 20%) and typically ranges between 1.0 and 1.1, indicating small intensity variations in the nebular background around our sources, which our procedure corrects.

In Figure 1, the examples of sources 9884 and 20408 illustrate the two cases of uniform and highly varying backgrounds. The outline of the three microshutters in the slitlet is shown on top of images in different bands, namely, H α (F658N) from the HST Advanced Camera for Surveys observations (E. Sabbi et al. 2007) and F444W from JWST NIRCcam observations (O. C. Jones et al. 2023; N. Habel et al. 2024). Since there are three nodding positions, in total five microshutters are shown in projection.

Our final goal is to correct the H recombination lines in our sources, i.e., to remove the signatures of the nebular background. Therefore, the uncertainty introduced by this procedure depends on how well the observed He I intensity variations match the variations in the H recombination lines. To assess this, we compare to one another the spectra of the two background microshutters (those above and below the

source, namely, “b” and “d” in Figure 1), after having registered them to have the same He I line flux. For the three prominent H recombination lines in our study, intensity variations range from 1% to 10%, with a typical difference of 5% for Pa α , 6% for Br γ , and 5% for Br β . For some targets, the He I line flux in the background spectra matches that in the source spectrum (within Poisson uncertainties), so no rescaling of the background spectrum is needed before subtraction. This is the case when the nebular background is rather constant around the source, like for source 9884, where the background level in the H α band is rather uniform in the four regions probed by the nodding pattern around the source. The situation is very different for source 20408, where simple background subtraction without rescaling would not be appropriate.

We finally note that, by design, our nodding strategy places the spectrum of the source and the background spectra at the same location on the detector and in the field of view, thereby avoiding uncertainties caused by possible flat-fielding and throughput mismatches as well as nonresponsive pixels.

After background subtraction, the spectra extracted from the three nodding positions of each source were median averaged to improve the SNR, and pixels flagged as saturated, nonlinear, or affected by high detector noise were excluded.

4. Spectroscopic Diagnostics and Physical Properties of the Stars

The background-subtracted and combined spectra are shown in Figure 2, while the derived physical parameters of the stars are listed in Table 1. The typical statistical uncertainty on the extracted spectra, after all pipeline steps and background subtraction, is $\sim 3 \times 10^{-20}\ \text{erg cm}^{-2}\ \text{s}^{-1}\ \text{\AA}^{-1}$. This is shown by the shaded areas around each spectrum in Figure 2. The corresponding SNR of the spectra (as defined by F. Stoeck et al. 2008) ranges from 3 for source 40571 to 42 for source 9884. The typical uncertainty (median value) and range (from the 17th to 83rd percentiles) of the measured line luminosities and EW are 2% (2%–5%) for Pa α , 6% (4%–12%) for Br β , and 9% (2%–16%) for Br γ and are dominated by the uncertainty on the level of the underlying continuum. The absolute calibration of the spectra is based on NIRCcam photometry in the F200W or F277W bands, which for our sources in the range of $20 < m_{200} < 24$ has a typical uncertainty of 0.1 mag or 10% (N. Habel et al. 2024).

All PMS candidates show prominent H recombination lines in their spectra, in particular Pa α and Br β (Br γ is also in emission). For some of the PMS candidates, Br δ and Br ϵ are also detected. Conversely, the spectra of MS stars show H absorption lines but no emission lines. No He I nebular lines are present in any of these spectra, confirming good nebular background subtraction (see Section 3). In Figure 3, we compare the spectrum of a PMS candidate of intermediate age (source 12559, ~ 12 Myr, black line) with a representative MS spectrum (red line) obtained as the mean of the three MS stars in our sample. Three H absorption lines are clearly present in the MS spectrum (Br ϵ , Pa α , Br δ), in contrast with the prominent emission features of the PMS star.

In this section, we discuss the physical properties derived from the spectra, starting from those of MS stars. We also discuss and quantify three types of spectral features that are characteristic of young stellar objects, namely, atomic H

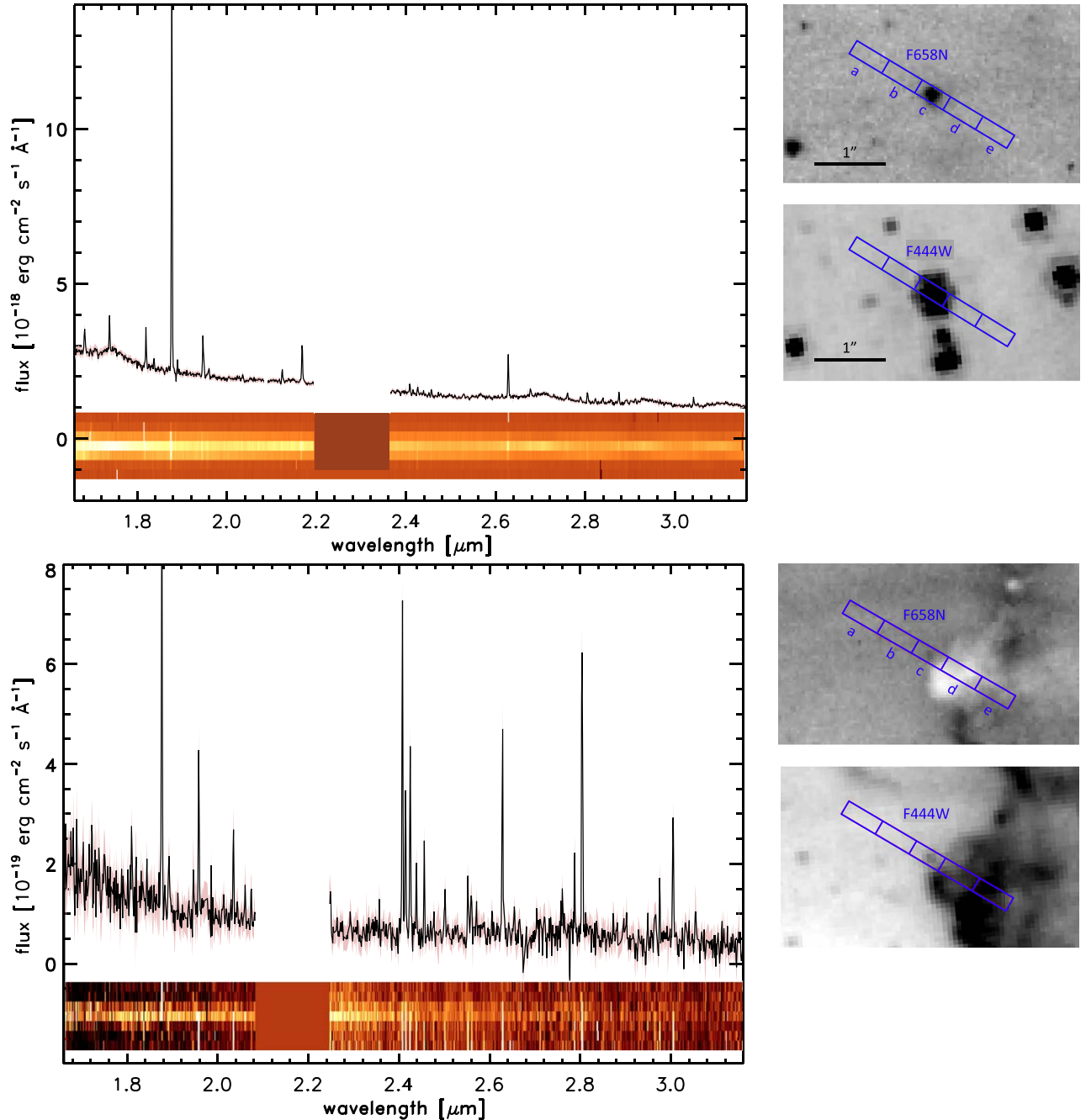


Figure 1. Spectra of sources 9884 (top panel) and 20408 (bottom panel). For each star, we display the 1D spectrum (after background subtraction) and associated 1σ uncertainties (which are derived from standard error propagation through the reduction pipeline). In the bottom panel, we show the 2D-rectified trace. The panels on the right-hand side show the HST F658N ($H\alpha$) and the NIRC2 F444W filter negative images, with the three nodding positions of the NIRS2 slitlet array aperture shown in blue. There are three nodding positions, namely “abc,” “bcd,” and “cde,” with the footprints of the five individual microshutters labeled a to e in the figure. Note that isolated bright pixels, such as those appearing in the 2D-rectified trace in the top panel near $1.8\ \mu\text{m}$ and $2.6\ \mu\text{m}$, are the result of flags in the pipeline processing to exclude spurious pixels (e.g., hot pixels, cosmic-ray hits, saturation, no linearity correction, etc.). Once flagged, the pixels are excluded from the analysis and do not have any effect on the extracted one-dimensional spectra (same panel in Figure 1) that are used in this work.

recombination lines, molecular H excitation lines, and continuum NIR excess.

4.1. Metallicity, Effective Temperature, and Surface Gravity

No absorption spectral features from elements other than H are seen in any of our spectra. In fact, they are not expected because of the low metallicity of NGC 346 and because of our limited resolving power ($R \sim 1000$). For illustration purposes,

the blue line in Figure 3 shows, as an example, the theoretical MS spectrum (P. H. Hauschildt et al. 1999) for a stellar photosphere with metallicity $[M/H] = -0.5$ and $T_{\text{eff}} = 7000\ \text{K}$, appropriate for these stars, and agrees well with the observations: no absorption lines other than those of H are present in the theoretical spectrum.

However, even without metal lines, we can set constraints on the effective temperature, surface gravity, and metallicity of the MS stars from the H absorption lines. To this end, we

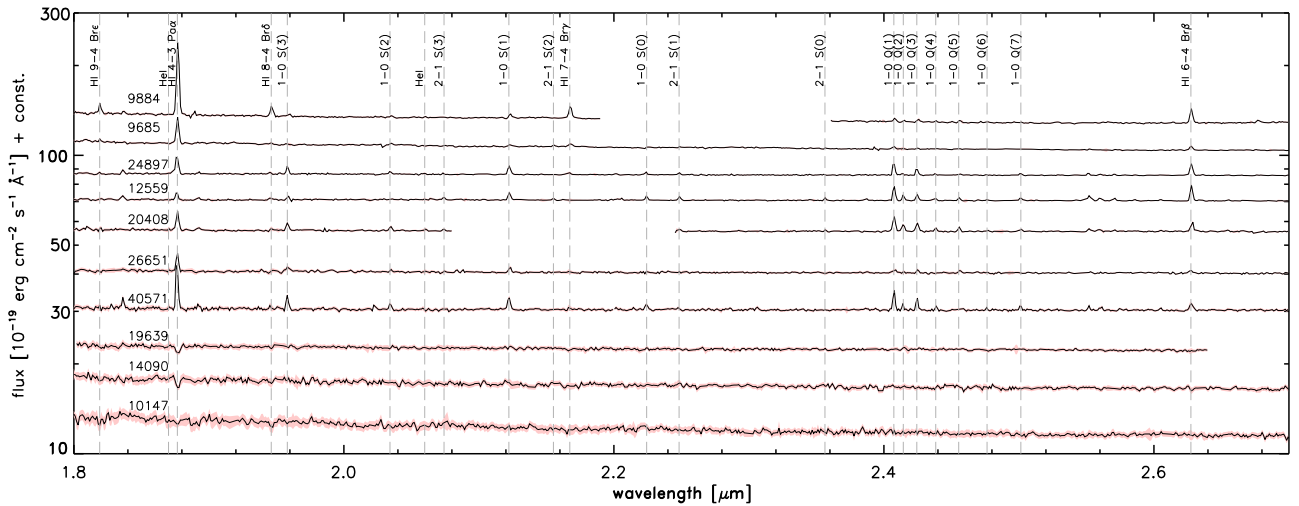


Figure 2. Calibrated, background-subtracted spectra of seven PMS and three MS representative stars. Object numbers correspond to Table 1. To improve visibility, the spectra are shifted vertically by offsets of $(11.5, 10, 8.5, 7, 5.5, 4, 3, 2.2, 1.6, 1.1) \times 10^{-18} \text{ erg cm}^{-2} \text{ s}^{-1} \text{ Å}^{-1}$. The vertical scale in this figure is compressed and the H absorption lines in the spectra of MS stars, although present, might be difficult to see. For a clearer view, see Figure 3.

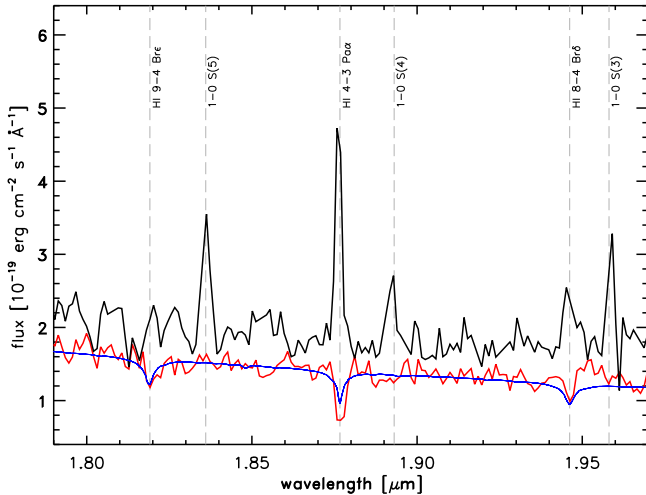


Figure 3. Comparison of PMS and MS spectra. The spectrum of PMS star 12559 (black line) is compared with the mean of the three MS spectra in our sample (red line), and with a model atmosphere with physical parameters appropriate for the MS objects (blue line).

compared the spectra of sources 10147 and 14090 with the F. Castelli & R. L. Kurucz (2003) model atmospheres (suitably convolved and resampled to match the spectral resolution of the G235M grating of NIRSpc) because they are most appropriate for our observations in the relevant range of T_{eff} probed by these stars. We also tested the MARCS models (B. Gustafsson et al. 2008) and obtained typical cross-model uncertainties of 0.5 dex in $[\text{Fe}/\text{H}]$, 200 K in T_{eff} , and 0.2 dex in $\log g$. We assumed a value of 2 km s^{-1} for microturbulence, which is appropriate for the T_{eff} and $\log g$ values of our targets. As for the line list, we used as a reference the Vienna Atomic Line Database (F. Kupka et al. 2011) in the range of $1.7\text{--}3.2 \mu\text{m}$. Both the MOOG (C. Sneden et al. 2012; version 2019) and Spectroscopy Made Easy (J. Valenti & N. Piskunov 1996; version 2020) radiative transfer codes were tested, and with both codes, we searched for the best fit in two ways: one in which the full wavelength range of $1.71\text{--}1.97 \mu\text{m}$ is fitted, and one in which only the observed H lines are considered (which,

unlike metal lines, are always clearly detected). In general, the MOOG code provides better fits.

For star 11047, when considering only H absorption lines in the stated range, the best fit is obtained for $T_{\text{eff}} = 8200 \pm 500 \text{ K}$, $\log g = 4.5 \pm 0.5$, and $-1.0 < [\text{Fe}/\text{H}] < -0.5$. When instead the fit is extended to the whole wavelength range of $1.71\text{--}1.97 \mu\text{m}$, the preferred values are $T_{\text{eff}} = 7700 \pm 300 \text{ K}$, $\log g = 4.4 \pm 0.5$, and $-1.0 < [\text{Fe}/\text{H}] < -0.5$. In both cases, $v \sin i$ cannot be constrained because our $\sim 300 \text{ km s}^{-1}$ resolution is too coarse. In both cases, solar metallicity can be excluded, but the lack of any metal lines does not allow us to set firmer constraints on the actual metallicity, other than to say that the range of $-1.0 < [\text{Fe}/\text{H}] < -0.5$ is consistent with the observations. However, we highlight here that the lack of metal lines applies to all sources in our sample, even the brightest ones for which the SNR in the continuum exceeds 30. This in itself is an indication that the metallicity is low.

In the case of star 14090, if only H absorption lines are considered, the parameter values providing the best fit are $T_{\text{eff}} = 7700 \pm 300 \text{ K}$, $\log g = 4.6 \pm 0.5$, and $-1.0 < [\text{Fe}/\text{H}] < -0.5$. If the complete $1.71\text{--}1.97 \mu\text{m}$ spectral range is considered, the values are $T_{\text{eff}} = 7500 \pm 400 \text{ K}$, $\log g = 4.3 \pm 0.5$, and $-1.0 < [\text{Fe}/\text{H}] < -0.5$. Also for this star can $v \sin i$ not be constrained.

We find that the values of T_{eff} and their uncertainties are fully consistent with those derived by G. De Marchi et al. (2011a) from the photometry of these stars in the V and I bands, as listed in Table 1. Furthermore, comparison of the corresponding model atmospheres (F. Castelli & R. L. Kurucz 2003) allows us to confirm also the values of A_V derived by G. De Marchi et al. (2011a) from the photometry (see Table 1 and Section 5). While we cannot use the same approach to set constraints on T_{eff} and the other stellar parameters for PMS stars because the H lines are in emission, the excellent match for MS stars gives us confidence about the photometrically derived T_{eff} also for the PMS sources in our sample.

4.2. H Recombination Lines and Mass Accretion

The prominent H emission lines in Figure 2 demonstrate for the first time that the NGC 346 stars with H α excess emission in HST photometry are indeed actively accreting PMS objects.

Table 2
Properties of the Stars in the Lupus and Taurus Sample

ID	Class	T_{eff} (K)	Age (Myr)	Mass (M_{\odot})	$W_{\text{Br}\gamma}$ (Å)	$W_{\text{Br}\zeta}$ (Å)	$W_{\text{Br}\eta}$ (Å)	$W_{\text{Pa}\beta}$ (Å)
RXJ1556.1-3655	II	3800	8	0.6	0.12 (0.03)
Sz122	III	3500	7	0.4	0.94 (0.14)
HQ Tau	II	5000	10	2.0	...	0.55 (0.06)	0.08 (0.05)	0.58 (0.08)
V1115 Tau	III	4500	10	1.0	...	0.24 (0.06)	0.14 (0.05)	0.25 (0.02)

Note. The columns correspond to the source identification (ID), class, effective temperature (T_{eff}), age, stellar mass (M_{\ast}), and EW of the $\text{Br}\gamma$, $\text{Br}\zeta$, and $\text{Pa}\beta$ lines (1σ uncertainties are shown in parenthesis). All spectral lines have positive EW, indicating absorption.

Following the relationships for a sample of 91 PMS objects in Lupus (J. M. Alcalá et al. 2017), we converted the $\text{Br}\gamma$ line luminosities $L(\text{Br}\gamma)$ of the PMS spectra, corrected for extinction, into the accretion luminosities $L_{\text{acc}}(\text{Br}\gamma)$ (for more details on the procedure see the Appendix and C. Rogers et al. 2024). In Table 1, these can be compared with the $L_{\text{acc}}(\text{H}\alpha)$ accretion luminosities obtained by applying the relationships of J. M. Alcalá et al. (2017) to the $L(\text{H}\alpha)$ line luminosities measured photometrically (G. De Marchi et al. 2011a) for the same objects. The uncertainty on the derived L_{acc} is about 0.25 dex (see J. M. Alcalá et al. 2017).

Except for stars 26651 and 12559, where the weak $\text{Br}\gamma$ line implies an uncertain luminosity, the two independent sets of $L_{\text{acc}}(\text{H}\alpha)$ and $L_{\text{acc}}(\text{Br}\gamma)$ values, based on measurements taken 18 yr apart, agree to better than a factor of 2, consistent with the accretion rate variability observed for PMS objects (G. F. Gahm et al. 2008; G. J. Herczeg et al. 2009; K. Biazzo et al. 2012; L. Venuti et al. 2014).

Using the available (G. De Marchi et al. 2011a) stellar masses and ages (Table 1), we can derive mass accretion rates (see the Appendix for the details). For stars older than ~ 10 Myr, the typical accretion rate is $\sim 10^{-8} M_{\odot} \text{ yr}^{-1}$, which is in good agreement with that estimated for similar objects in the Magellanic Clouds (G. De Marchi et al. 2010, 2011a, 2013, 2017; K. Biazzo et al. 2019; R. Carini et al. 2022; M. Vlasblom & G. De Marchi 2023; S. Tsilia et al. 2023), and yet about an order of magnitude larger than for stars of similar mass and age in nearby Galactic star-forming regions (L. Hartmann et al. 2016).

A preliminary comparison of the observed line ratios to those predicted by temperature- and electron-density-dependent models (P. J. Storey & D. G. Hummer 1995) for case B hydrogen recombination (J. G. Baker & D. H. Menzel 1938) suggests $T_{\text{eff}} \simeq 5000$ K and $N_e \simeq 10^{10} \text{ cm}^{-3}$. These values are consistent with those predicted by magnetospheric accretion models for classical T Tauri stars (S. C. Martin 1996; J. Muzerolle et al. 1998), although the temperature is slightly lower than the 6000–12,000 K range predicted by J. Muzerolle et al. (2001).

4.2.1. Comparison with Older Galactic PMS Stars

We have compared the IR spectra of the older PMS sources in NGC 346 with those of ~ 10 Myr old stars in two Milky Way star-forming regions, Taurus and Lupus. We selected two sources in Taurus (HQ Tau and V1115 Tau) and two in Lupus (RXJ1556.1-3655 and Sz122) with ages in that range. The spectra of the sources in Taurus come from TNG/GIARPS NIR observations (J. M. Alcalá et al. 2021) and the corresponding physical parameters were derived by M. Gangi et al. (2022). The NIR spectra of the sources in Lupus are taken from Very Large Telescope/XSHOOTER observations

(J. M. Alcalá et al. 2014, 2017) and the physical parameters of the sources are discussed in A. Frasca et al. (2017). The PMS nature of these Taurus and Lupus sources was assessed by those authors on the basis of the NIR excess and the ages were determined by comparing the stellar photometry with theoretical PMS isochrones, which is the same approach followed for the NGC 346 sources (G. De Marchi et al. 2011a and Section 5).

Table 2 summarizes the physical parameters of the four Milky Way sources (as published in the papers mentioned above), to which we have added the EW of some representative H recombination lines in the NIR, as measured by us on the calibrated background-subtracted spectra provided in those papers.

The XSHOOTER spectra of the sources in Lupus sample the $\text{Br}\gamma$ line. For both objects, the line is found to be in absorption, with EW of 0.12 Å (with 1σ uncertainty of 0.03 Å) for RXJ1556.1-3655 and 0.94 Å (0.12 Å) for Sz122. The GIARPS spectra of the Taurus sources do not sample $\text{Br}\gamma$, so we looked at nearby H recombination lines, starting from $\text{Br}\zeta$ ($\text{Br}-10$ at $1.736 \mu\text{m}$, which is also covered in the NIRSpect spectra but is too faint for our sources, except for 9884 and 9685). This line is also seen in absorption, with EWs of 0.55 Å and 0.24 Å for HQ Tau and V1115 Tau, respectively. Since telluric lines are very pronounced around $\text{Br}\zeta$, and some residual absorption might remain even after subtraction, we also inspected the $\text{Br}\eta$ ($\text{Br}11$ at $1.681 \mu\text{m}$) and $\text{Pa}\beta$ lines (not included in the NIRSpect spectra of the NGC 346 sources). The $\text{Br}\eta$ and $\text{Pa}\beta$ lines are also in this case clearly seen in absorption, with EWs of 0.08 Å and 0.55 Å for HQ Tau and 0.14 Å and 0.25 Å for V1115 Tau, respectively. As a result, we expect that also $\text{Br}\gamma$ and $\text{Pa}\alpha$ will be in the absorption for these sources.

On the other hand, objects with comparable ages in NGC 346 (ID 24897, 12559, and 20408) show strong emission in the $\text{Br}\gamma$ and $\text{Pa}\alpha$ lines, with EWs of order 10 Å for $\text{Br}\gamma$ and hundreds of angstroms for $\text{Pa}\alpha$, clearly indicating that the stars are still accreting material from the circumstellar environment. In summary, while PMS stars with ages of about 10 Myr show strong signs of accretion in NGC 346, no such signs are detected in stars of similar age in small nearby Galactic star-forming regions with solar metallicity.

4.3. H_2 Excitation Lines and Outflows

The background-subtracted spectra of the PMS stars in Figure 2 reveal a conspicuous number of molecular hydrogen (H_2) excitation lines. In particular, the lines corresponding to the rovibrational transitions $v = 1 \rightarrow 0$ S(0), $1 \rightarrow 0$ S(1), $1 \rightarrow 0$ S(2), $1 \rightarrow 0$ S(3), $2 \rightarrow 1$ S(1), $2 \rightarrow 1$ S(2), $2 \rightarrow 1$ S(3), as well as $1 \rightarrow 0$ Q(1) through to $1 \rightarrow 0$ Q(7) are observed. Since the

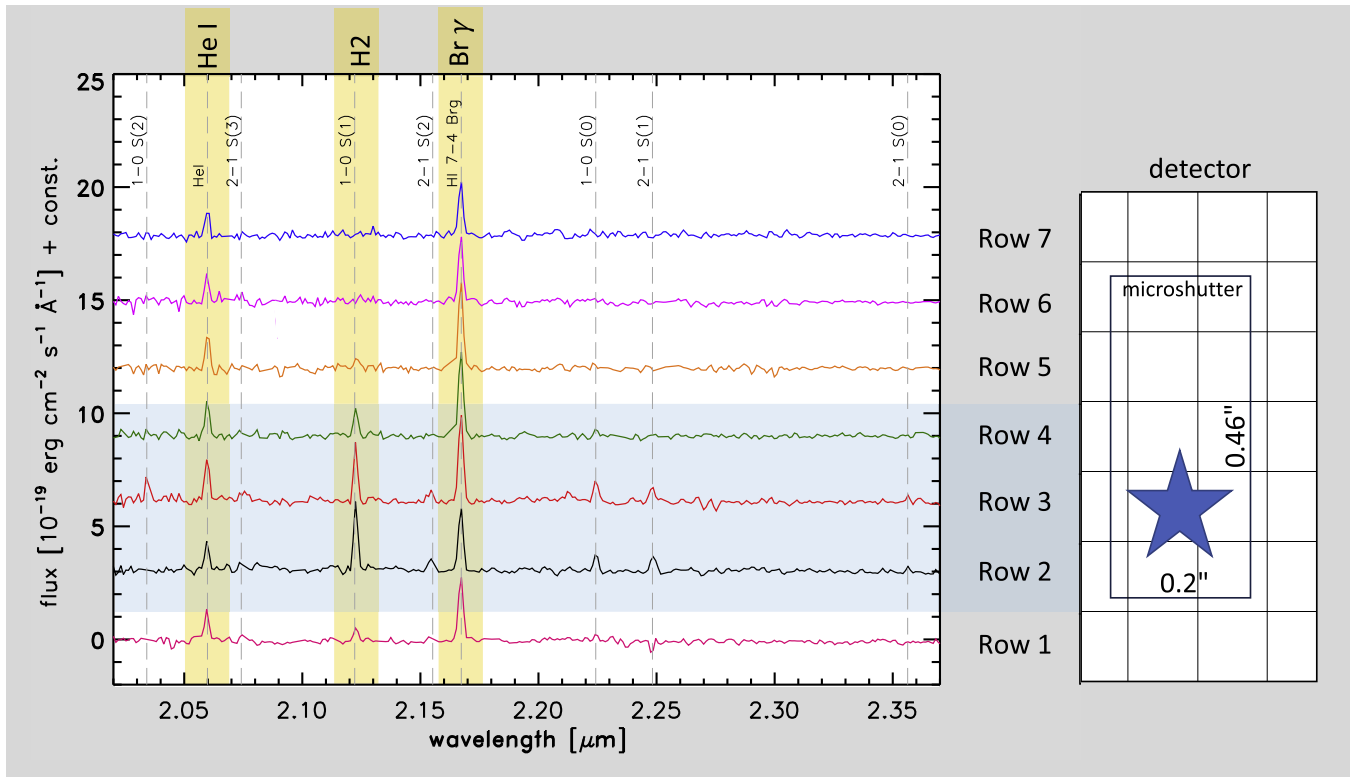


Figure 4. Localized H_2 excitation lines around source 40571. Left: source spectra along the seven individual pixel rows of the rectified trace, without background subtraction. Right: projected position of the source in the microshutter. The $\nu = 1 \rightarrow 0$ S(1) excitation line is stronger at the specific location of the source, while nebular lines are present across the full slit length.

spectra are background subtracted, the molecular gas must be spatially associated with the stars.

By knowing the exact location of the stars in the microshutter, we can set constraints on the distribution of the H_2 molecular material. Figure 4 shows the spectra of source 40571, without background subtraction; the side panel indicates the position of the source inside the microshutter (as provided by the MSA configuration file), which is intermediate between pixel rows 2 and 3 in the extracted rectified trace (note that rows 1 and 7 of the trace are only partly illuminated). While the He I and Br γ nebular emission lines extend across the full height of the slit, the spatial extent of the $\nu = 1 \rightarrow 0$ S(1) emission line is more limited around the specific location of the source. The same is true for the other six PMS candidates, indicating that H_2 is likely associated with circumstellar material.

The extent of the H_2 emission in the spatial direction is about $0''.1$ (1 pixel) and is not resolved. Therefore, we can only set an upper limit to the extent of the H_2 circumstellar structure (possibly an outflow in the disk or a filament), which at the distance of NGC 346 corresponds to ~ 6000 au. This is clearly just an upper limit, and we cannot set any constraints on the shape or structure at the origin of the H_2 emission, but we note that this size is within a few times the typical $\lesssim 1000$ au size of disks around Galactic PMS stars measured in Taurus (J. R. Najita & E. A. Bergin 2018).

Some of these H_2 lines are observable from the ground in nearby protostars and their intensity ratios are used to characterize the physical conditions and excitation mechanism in their circumstellar environments (T. P. Greene et al. 2010). Here, we provide a preliminary characterization of the environments and excitation mechanisms from the intensity

ratios of the S(1) lines in the $\nu = 2 \rightarrow 1$ and $\nu = 1 \rightarrow 0$ transitions. For star 12559, the intensity ratio is 0.47, suggesting nonthermal ultraviolet electron pumping, for which R. Gredel & A. Dalgarno (1995) predict a ratio of 0.54 (the value is higher if extinction is present). The intensity ratio of the S(3) lines in the $\nu = 2 \rightarrow 1$ and $\nu = 1 \rightarrow 0$ transitions agree with this scenario. For stars 9685, 24897, and 40571, the ratios are in the range of 0.11–0.18, characteristic of LTE molecular gas at temperatures of ~ 2200 – 2700 K, as commonly seen in shocks from outflows. Stars 26651, 9984, and 20408 were analyzed for the $2 \rightarrow 1$ S(3) line ratio because the S(1) line was affected by bad pixels or not covered in the wavelength range of the spectra. These three stars also have line ratios consistent with the shock excitation of H_2 gas in LTE at ~ 2200 – 2700 K.

In summary, the intensity ratios of the S(1) and S(3) lines in the $\nu = 2 \rightarrow 1$ and $\nu = 1 \rightarrow 0$ transitions suggest that the likely excitation mechanism for one of the stars (12559) is ultraviolet electron pumping, while for the other objects shocks appear to be the cause. The measured H_2 line ratios in these stars point to excitation mechanisms that likely trace a variation in underlying physical processes from outflows and circumstellar disk material commonly seen in young stars in the Milky Way.

4.4. NIR Excess and Circumstellar Dust

Finally, the spectral energy distributions (SEDs) of the PMS stars in our sample present NIR excess caused by dust emission, which provides additional evidence of the presence of circumstellar disks. In Figure 5, we compare the SEDs of the stars obtained by fitting the continuum of the spectra in Figure 2 using a linear interpolation with a step of $\sim 0.1 \mu\text{m}$. The derived SEDs were corrected for reddening, using the A_V

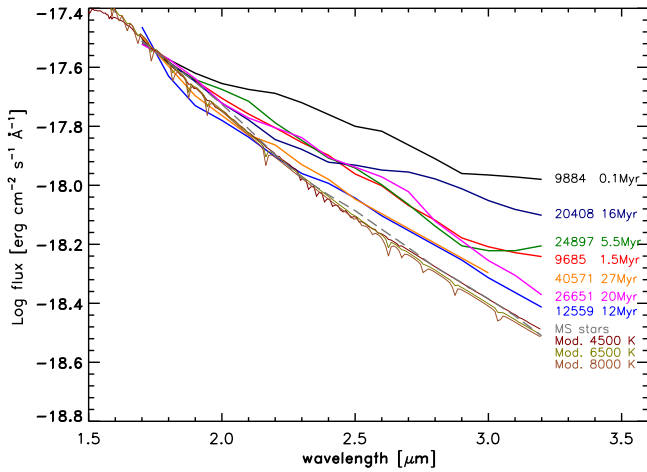


Figure 5. SEDs (fitted continua) of the dereddened sources registered at $1.75 \mu\text{m}$. The spectra of PMS stars are shown individually (thick color lines as per the legend), while the three MS stars are averaged together (gray dashed line), as in Figure 3. The thin lines correspond to theoretical model spectra for metallicity $[M/H] = -0.5$ and $T_{\text{eff}} = 4500 \text{ K}$, 6500 K , and 8000 K , respectively.

values in Table 1 with the extinction law of G. H. Rieke & M. J. Lebofsky (1985), and are normalized at $1.75 \mu\text{m}$ for comparison. The gray dashed line corresponds to the average MS star spectrum shown in Figure 5 and closely matches the model spectra (M. S. Bessell et al. 1998) for metallicity $[M/H] = -0.5$, surface gravity $\log g = 4.5$ and T_{eff} of 4500 K , 6500 K , and 8000 K (see the legend). This comparison confirms that in this wavelength and temperature range the spectral shape in the Planck tail of the distribution is not particularly sensitive to the exact T_{eff} value. The differences observed in the SEDs of the PMS stars, with respect to those of the MS objects, clearly indicate the presence of NIR excess. This further confirms that the stars with excess emission in the H recombination lines are not standard MS stars. If their continuum matched that of MS stars, the emission lines might simply be the result of an incomplete subtraction of the nebular background. Instead, the markedly different continuum shape provides independent evidence that these objects are not MS stars and are still surrounded by circumstellar material.

All PMS candidates except for source 12559 reveal NIR excess also in the NIRCcam photometric bands F115W, F200W, and F277W (N. Habel et al. 2024), with excess values ranging from 0.25 to 1.3 mag compared to the colors of the MS stars in our sample. In general terms (see Table 1), younger PMS candidates have typically larger NIR excess, with some scatter. The scatter, however, is not surprising: although the mass of the circumstellar disk decreases over time, the amount of NIR excess does not directly scale with age because of the effects introduced by different disk geometry and morphology, including inclination (A. Garufi et al. 2018). For instance, the presence of spirals and shadows is associated with a high NIR excess, while the presence of rings in the disks appears to cause low NIR excess (A. Garufi et al. 2018), irrespective of the actual PMS age. Therefore, a pronounced NIR excess for an older PMS candidate, like star 20408, can be expected.

5. Discussion: A Matter of Age

In this section, we discuss the ages of the PMS stars in our sample, how they were derived from the photometry and their

uncertainties. Some elements of this discussion have been presented by G. De Marchi et al. (2011a), but here we address the matter in more detail and through a number of independent arguments, all of which point to an old age for a significant fraction of the accreting PMS stars in NGC 346.

A search for PMS stars in NGC 346 (G. De Marchi et al. 2011a) revealed approximately ~ 690 candidates with strong H α excess emission in their photometry, corresponding to H α EW $> 20 \text{ \AA}$. In the V , $V-I$ CMD, after reddening correction, these PMS candidates form two distinct groups, a red group and a blue group, with a median $V-I$ color separation of 0.75 mag at all magnitudes. When the T_{eff} and L_{bol} of these stars, derived from the photometry, are compared in the Hertzsprung–Russell (H-R) diagram with widely used PMS models (L. Siess et al. 2000; E. Tognelli et al. 2011; J. Tang et al. 2014), the 0.75 mag color separation translates into a clearly bimodal age distribution, with about half of the objects younger than $\sim 2 \text{ Myr}$ and the other half older than $\sim 8 \text{ Myr}$, including over 200 stars with ages in the range of $15\text{--}30 \text{ Myr}$. To help readers appreciate the systematically different locations of the younger and older PMS candidates in the CMD and H-R diagram, we have included in the left and right panels of Figure 6, respectively, the CMD and the H-R diagram as published by G. De Marchi et al. (2011a), with those authors’ permission. These figures are relevant because they were used to select the spectroscopic targets for the investigation reported here.

Hereafter, we will refer to these two groups of PMS stars as “older PMS candidates” and “younger PMS candidates,” respectively. The former include the stars with H α excess emission in Figure 6 with color $0.1 \lesssim V-I \lesssim 0.8$, which G. De Marchi et al. (2011a) showed to be older than $\sim 8 \text{ Myr}$ (median age 20 Myr), to have masses in the range of $0.7\text{--}1.5 M_{\odot}$, and to be located primarily in the outskirts of the association. The latter include objects with H α excess emission in Figure 6 with color $0.8 \lesssim V-I \lesssim 2.0$, younger than $\sim 2 \text{ Myr}$ (median age 0.9 Myr), with masses in the range of $0.4\text{--}4.0 M_{\odot}$, and located near the center of the association, in compact subclusters.

In the following subsections, we address three specific points, which are however intertwined, namely, the location of the PMS sources in the CMD, their reddening, and their spatial distribution. We also explore how representative the older emitting PMS sources are of the older PMS population in NGC 346 as a whole.

5.1. CMD and Photometric Uncertainties

Here, we discuss the location of the PMS sources in the CMD and show that their small photometric uncertainties, combined with the low metallicity of the NGC 346 cluster, allow us to set stringent constraints on the relative ages of the younger and older PMS stars.

The typical photometric uncertainty in the V and I bands for the PMS stars in the catalog of E. Sabbi et al. (2007) used by G. De Marchi et al. (2011a) is 0.02 mag , which translates into typical uncertainties of about $1\%\text{--}2\%$ on T_{eff} and of $\sim 6\%$ on L_{bol} . In that work, the value of T_{eff} was derived by comparing the observed $V-I$ color, after correction for reddening, with those stemming from the model atmosphere of M. S. Bessell et al. (1998) for metallicity $[M/H] = -1.0$ and gravity $\log g = 4.5$, as appropriate for the PMS sources in NGC 346, and for the specific HST bands used in those observations (see G. De Marchi et al. 2010, 2011a for details). The stellar

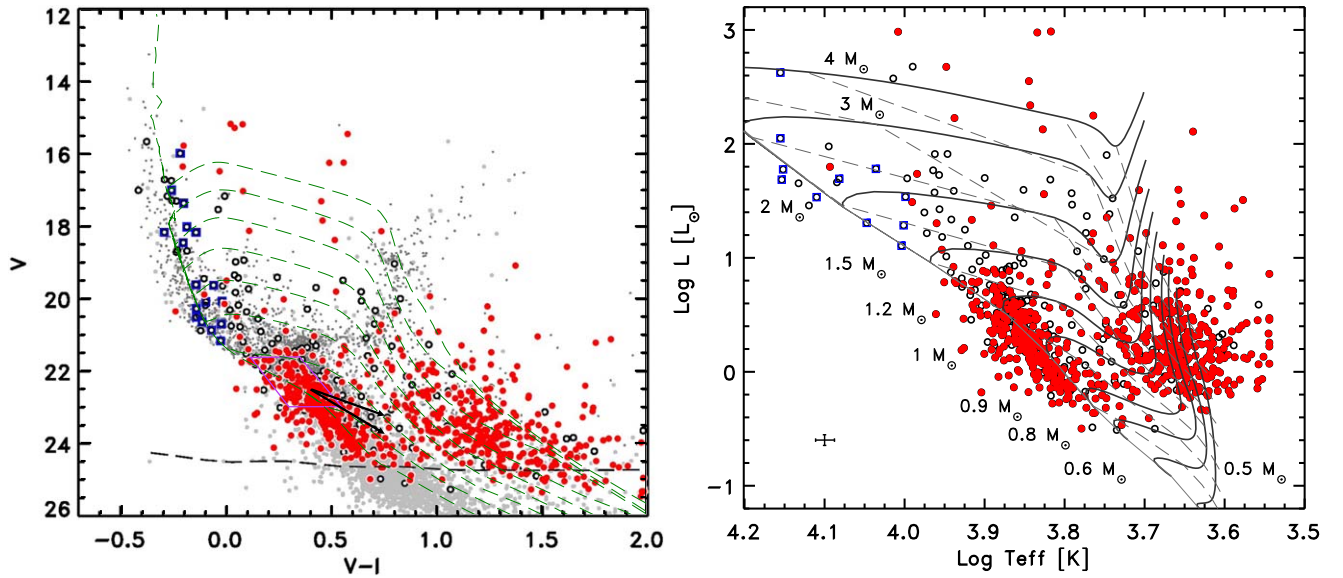


Figure 6. Left: CMD of the stars in NGC 346 (G. De Marchi et al. 2011a). All magnitudes are corrected for extinction. Objects with excess emission in $H\alpha$ at the 4σ level or higher are shown as open circles. A total of 694 of them (red dots) also have $H\alpha$ excess emission with EW in excess of 20 \AA or more than 50 \AA for stars hotter than $10,000 \text{ K}$. Squares correspond to objects with $H\alpha$ excess emission and EW of less than 50 \AA that are potential Be stars. The thick black dashed line corresponds to the 50% completeness limit of the photometry in the V and I bands (E. Sabbi et al. 2007). The majority of other stars in the field (gray dots) do not show $H\alpha$ excess emission. Thin green dashed lines correspond to isochrones from J. Tang et al. (2014) for $Z = 0.002$ and ages of 0.125, 0.25, 0.5, 1, 2, 4, 8, 16, and 32 Myr from right to left. The arrows show representative reddening vectors for color excess $E(V - I) = 0.5$ and two values of the total-to-selective extinction ratio: $R = 3.1$ (standard Galactic extinction law, top arrow), and $R = 4.5$ as measured in the low-metallicity massive starburst cluster 30 Dor (bottom arrow). Right panel: H-R diagram of the stars with $H\alpha$ excess at the 4σ level or higher. Thick solid lines show the evolutionary tracks from the Pisa group (S. Degl’Innocenti et al. 2008; E. Tognelli et al. 2011) for metallicity $Z = 0.002$ and masses from 0.5 to $4 M_{\odot}$, as indicated. The corresponding isochrones are shown as thin dashed lines, for the same ages as in the left panel. Note that the constant logarithmic age step has been selected such that the typical distance between isochrones is larger than the uncertainties (indicated by the typical error bars in the bottom-left corner of the H-R diagram). The purple polygon is discussed in Section 5.4.

parameters derived spectroscopically in Section 4 attest to the accuracy of the effective temperature obtained from the photometry. Bolometric luminosities are based on the adopted SMC distance modulus of 18.92 ± 0.03 , corresponding to $\sim 61 \text{ kpc}$ (R. W. Hilditch et al. 2005; S. C. Keller & P. R. Wood 2006). While it has long been known that the SMC extends about 5 kpc along the line of sight (e.g., L. T. Gardiner & M. R. S. Hawkins 1991; D. Nidever et al. 2011; P. Yanchulova Merica-Jones et al. 2017; C. E. Murray et al. 2024), there is no evidence that this is the case for the specific NGC 346 star-forming region. The diameter of the region is about 60 pc , and one expects the extent along the line of sight to be similar. This will have no measurable effects on the dispersion in the photometry and hence on the derived value of L_{bol} .

Figure 6 shows that older PMS candidates with $H\alpha$ excess emission (which here we show to have excess emission also in the Paschen and Brackett lines) appear very close to the location of the MS, shown by the solid gray line in the right panel of Figure 6. Objects of this type are not observed in nearby Galactic star-forming regions. However, their position in the H-R diagram is fully consistent with theoretical models of stellar evolution in low-metallicity environments. At the metallicity of NGC 346 ($Z = 1/8 Z_{\odot}$ or $Z \simeq 0.002$), theoretical evolutionary tracks (S. Degl’Innocenti et al. 2008; E. Tognelli et al. 2011) show that a $1 M_{\odot}$ star reaches the MS after about 20 Myr , as we illustrate in Figure 7. The time is about 27 Myr for a $0.9 M_{\odot}$ object like source 40571 in Table 1. At solar metallicity, models by the same authors show that this time is twice as long, or about 43 Myr for a $1 M_{\odot}$ star. We verified that both the MIST (A. Dotter 2016) and PARSEC (A. Bressan

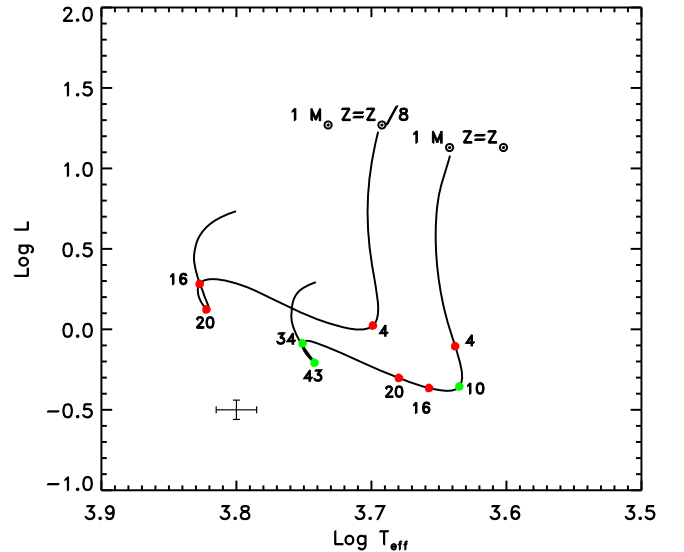


Figure 7. PMS evolutionary tracks from E. Tognelli et al. (2011) for a $1 M_{\odot}$ star and two different metallicities, as indicated. Numbers along the tracks correspond to PMS ages in Myr. At $Z = 1/8 Z_{\odot}$, the transition from the bottom of the Hayashi track to the MS occurs earlier and more rapidly than at Z_{\odot} . For reference, we also show the error bars from the right panel of Figure 6.

et al. 2012) evolutionary tracks would produce very similar results.

More importantly, even if the lifetime of circumstellar disks did not depend on metallicity, Figure 7 implies that in low-metallicity environments there is a higher probability of finding PMS stars close to the MS, which are still actively accreting. Indeed, photometric investigations of star-forming regions across the Magellanic Clouds have systematically shown this

result over the past decade (G. De Marchi et al. 2010, 2011a, 2011b, 2013, 2017; K. Biazzo et al. 2019; R. Carini et al. 2022; S. Tsilia et al. 2023; M. Vlasblom & G. De Marchi 2023). Obviously, if disk lifetimes increase at lower metallicity, as our observations appear to indicate (see Section 6), the likelihood of finding still accreting PMS stars close to the MS is even higher.

Figure 7 presents an additional important implication for uncertainties on ages, which are derived through isochrone comparison and as such are affected by uncertainties on T_{eff} and L_{bol} . The latter in turn depend on uncertainties in the photometry and on the extinction correction (typical uncertainties on $\log T_{\text{eff}}$ and $\log L_{\text{bol}}$ are shown by the error bars in Figure 7). None of these uncertainties depend on metallicity. Since at lower metallicity stars transit more quickly across the H-R diagram, a given uncertainty on $\log T_{\text{eff}}$ and $\log L_{\text{bol}}$ will translate into a lower uncertainty on the age. We quantify this in Figure 7, where PMS evolutionary tracks for $1 M_{\odot}$ stars and two metallicities are compared. At $Z = 1/8 Z_{\odot}$, the star leaves the bottom of the Hayashi track at $t = 4$ Myr and reaches the MS region 12 Myr later, having become about 1500 K warmer, at an average rate of 150 K Myr^{-1} . At solar metallicity, the time spent on the radiative part of the PMS track is 24 Myr and T_{eff} increases by about 1300 K, so the average transfer rate is about 55 K Myr^{-1} . During the transfer phase, which accounts for the majority of the PMS lifetime, age uncertainties are about three times smaller at $Z = 1/8 Z_{\odot}$ than at solar metallicity (the actual factors, for a $1 M_{\odot}$ star, are 2.7, 2.5, and 2.6 for the PISA, MIST, and PARSEC tracks, respectively). This analysis shows that PMS stars in NGC 346 form two distinct age groups.

5.2. Reddening

One might suppose that the two groups of PMS candidate stars in the CMD and H-R diagram of Figure 6 belong in fact to the same population (i.e., have the same age) but simply appear in different regions of the CMD because they are affected by different reddening values, which have not been properly corrected. In the following, we show why this is not the case.

First of all, the extinction in this field is very limited, as the shape of the red clump (RC) indicates (see CMD in Figure 6). This was shown by G. De Marchi et al. (2011a), who inspected the photometry of ~ 600 massive stars in the cluster and derived the $E(V-I)$ color excess for each of them, and by N. Habel et al. (2024), who found tightly constrained RCs in near- and mid-infrared CMDs with JWST photometry. Since PMS candidates and massive stars have a similar spatial distribution in this field, G. De Marchi et al. (2011a) derived a statistical reddening correction for each PMS candidate from the median value of the extinction toward the five nearest massive star neighbors. That study showed that, even though some differential reddening is present in the field, with $E(V-I)$ ranging from 0.1 to 0.25 mag (17th and 83rd percentiles, respectively), the $V-I$ color separation between red and blue PMS stars in the CMD of Figure 6 is five times wider than the median color excess in the field, $E(V-I) \simeq 0.16$. These values are in turn consistent with those reported by E. Hennekemper et al. (2008), who found A_V in the range of 0.2–0.4 mag in the densest central regions.

The arrows in the CMD show the reddening vectors for two extinction laws: the one for the standard diffuse Galactic interstellar medium (e.g., J. A. Cardelli et al. 1989; E. Fitzpatrick 1999), with $R = 3.1$ corresponding to $A_V = 1.7 \times E(V-I)$, is shown by the

upper arrow; the lower arrow corresponds to the extinction law measured in the massive starburst cluster 30 Dor in the Large Magellanic Cloud (G. De Marchi & N. Panagia 2014; J. Maiz Apellaniz et al. 2014; G. De Marchi et al. 2016; K. Fahrion & G. De Marchi 2023), with $R = 4.5$ corresponding to $A_V = 3.0 \times E(V-I)$. The latter is likely to be more typical of starburst regions, in particular at low metallicity. It is clear that reddening cannot displace PMS stars from one group to the other within the observed magnitude range since in the CMD the reddening vectors run parallel to the separation between the two groups (note that, to improve visibility, the vectors are shown for $E(V-I) = 0.5$ or three times the median value in the field). To bridge the two groups, an unusually shallow reddening vector would need to be invoked, $A_V = 1.1 \times E(V-I)$. Furthermore, extinction can only shift objects to redder colors and fainter magnitudes in the CMD; therefore, the bluer stars can only have less extinction than the red ones, not more. So, the older PMS ages derived for the bluer stars cannot be attributed to insufficient reddening correction. In other words, if the reddening correction were insufficient, the ages would be underestimated, but less so for a steep reddening vector.

5.3. Spatial Distribution of Younger and Older PMS Stars

Also the spatial location of the PMS stars in the field suggests an intrinsic physical difference between the two groups of PMS candidates in Figure 6. In theory, episodic accretion in the early stages of evolution could make a small fraction of PMS stars appear bluer in the CMD, thereby mimicking an older age (I. Baraffe et al. 2009, 2017; I. Baraffe & G. Chabrier 2010; E. I. Vorobyov et al. 2013; M. Kuffmeier et al. 2018). However, G. De Marchi et al. (2011b) showed that the spatial distribution of the redder PMS stars is different from that of the bluer PMS objects: the former are more centrally concentrated and coincide with the small subclusters identified by E. Sabbi et al. (2007), while the latter are more widely distributed and not associated with the subclusters. Similar results were found using JWST photometry (O. C. Jones et al. 2023). Recently, E. Sabbi et al. (2022) demonstrated that the two populations also exhibit different kinematic patterns.

Therefore, in NGC 346 we can exclude episodic accretion as the main cause of the two separate groups of PMS objects in Figure 6, owing to the spatial segregation of the two groups in the field. Indeed, it is difficult to see how this effect, which must apply with equal probability to all stars regardless of their position in space, could explain the correlation observed between the colors of PMS stars and their spatial location in the cloud. We conclude that the two groups of PMS stars are not members of the same population and their clearly distinct positions in the CMD can only be explained by a difference in age.

5.4. Accreting and Nonaccreting Older PMS Stars

A final question is whether the older PMS sources with strong hydrogen emission are typical of the older PMS population of NGC 346 as a whole, or whether they represent the tail of a larger distribution of coeval stars that are no longer accreting, such as, for instance, in the case of the ~ 15 Myr old TW Hya (G. J. Herczeg & L. A. Hillenbrand 2014). To address this question, we turn to the sample of 330 NGC 346 PMS stars older than 8 Myr and with $H\alpha$ EW larger than 20 \AA as identified photometrically by G. De Marchi et al. (2011a). This

stringent selection inevitably leaves out some similarly aged sources that are weakly accreting or no longer accreting.

Since the area observed with HST around NGC 346 (E. Sabbi et al. 2007; G. De Marchi et al. 2011a) is dominated by SMC field stars, in order to limit statistical fluctuations, we focus our analysis on the region where the density of older PMS stars is higher. We defined an ellipsoidal region near the center of NGC 346 in such a way as to contain 50% of the older PMS candidates. The region spans about 3 square arcmin. We further restrict the sample by considering stars with $V < 23$ since this ensures completeness better than 50% in the V , I , and $H\alpha$ bands. A total of 63 PMS stars satisfy this additional condition and in the V , $V-I$ CMD they occupy an area containing an additional 483 sources with no $H\alpha$ excess emission (the area is outlined by the purple polygon in the left panel of Figure 6).

If all the 483 sources were nonaccreting PMS members of NGC 346, this would imply a $\sim 12\%$ fraction of accreting PMS objects at ages of 10–30 Myr. Given that many of these objects are likely to be SMC field stars, not related to the NGC 346 cluster, this is a lower limit and suggests that the older accreting PMS stars are significantly more than a tail in the distribution.

A proper determination of the actual fraction of accreting PMS stars requires a detailed statistical analysis of the field star contamination, including a thorough assessment of the photometric completeness and extinction, both of which are known to vary across the field (E. Sabbi et al. 2007; E. Hennekemper et al. 2008). The study is beyond the scope of this paper and we plan to undertake it in a future work.

6. Conclusions

Thanks to the excellent combination of sensitivity and spatial resolution of NIRSpec on JWST, we have been able to observe spectroscopically a sample of extragalactic solar-mass candidate PMS stars for the first time. The candidates were identified through $H\alpha$ excess emission in their photometry. Our new data set confirms that these objects are indeed PMS stars, with the spectral signatures of active accretion and the presence of colder molecular gas and of dust in circumstellar material. The spectroscopic confirmation of the PMS nature of the photometrically selected candidates suggests that it will be possible to extend the use of narrowband imaging methods to reliably identify and study star-forming objects in a variety of environments, also in galaxies further away in the Local Group.

The spectral features presented in Section 4 are common to both younger and older PMS stars in our sample, with ages spanning from ~ 0.1 to ~ 30 Myr. Independently of the age spread, all our objects reveal typical PMS signatures: prominent H recombination lines implying large accretion luminosities, H_2 excitation lines suggesting molecular material in the immediate vicinity of the stars, and NIR excess witnessing the presence of dusty circumstellar disks. This suggests that in NGC 346 circumstellar disks live longer than typical disks in the Milky Way and PMS stars can accrete at sustained rates for over 20 Myr. This is in contrast with what is observed in the Milky Way, where at solar metallicity, disks around stars of $\sim 1 M_\odot$ dissipate very quickly (S. Pfalzner et al. 2022).

Our results could appear to be at odds with the outcome of a study of two small low-metallicity ($\sim 0.1 Z_\odot$) star-forming regions in the extreme outer Galaxy (C. Yasui et al. 2009, 2010), where a

small fraction of sources with NIR excess suggested very short disk lifetimes, even shorter than in the solar neighborhood. However, subsequent studies of other low-metallicity Galactic clusters indicate that the actual fraction of disk-bearing stars in the outer Galaxy is controversial (F. Cusano et al. 2011; C. Yasui et al. 2016) and subject to large age uncertainties (M. G. Guarcello et al. 2021). Nor is it yet clear what is the exact role of stellar feedback on the evolution and lifetime of circumstellar disks. M. C. Ramirez-Tannus et al. (2023) studied circumstellar disks in the massive Galactic cluster NGC 6357: while they were expecting the disks to be more affected by the UV radiation from massive stars than in the much smaller Lupus star-forming region, the authors found that the spectra in the two regions are quite similar.

Thus, from an observational point of view, there is currently no compelling reason to believe that at low metallicity circumstellar disks are short-lived. Furthermore, the prevailing theories requiring short lifetimes appear to be problematic for the formation of the planets known to exist around low-metallicity stars (S. Sigurdsson et al. 2003; A. Niedzielski et al. 2009; J. Setiawan et al. 2010), and might question the validity of the core-accretion model for the formation of planetesimals (J. L. Johnson & H. Li 2012). For planets to form, dust must settle in the midplane before the disk dissipates, but the settling timescale is longer at the low dust-to-gas ratios expected in these environments and it increases with distance from the star. If disk dissipation in low-metallicity stars were as quick as initially reported (C. Yasui et al. 2009), only very small rocky planets close to the star could form (J. L. Johnson & H. Li 2012).

In conclusion, our results indicate that, at the low metallicities typical of the early Universe, the disk lifetimes may be longer than what is observed in nearby star-forming regions, thus allowing more time for giant planets to form and grow than in higher-metallicity environments. This may have significant implications for our understanding of the formation of planetary systems in environments similar to those in place at Cosmic Noon.

Acknowledgments

We are very grateful to an anonymous referee for providing insightful and stimulating comments that have helped us improve the presentation of our results. This work is based on observations made with the NASA/ESA/CSA James Webb Space Telescope. The data were obtained from the Mikulski Archive for Space Telescopes at the Space Telescope Science Institute, which is operated by the Association of Universities for Research in Astronomy, Inc., under NASA contract NAS 5-03127 for JWST. These observations are associated with program JWST-GTO-1227. The specific observations analyzed in this work can be accessed via doi:10.17909/tatn-1114. M.M. and N.H. acknowledge support through a NASA/JWST grant 80NSSC22K0025, and M.M., N.H., and L.L. acknowledge support from the NSF through grant 2054178. O.N. acknowledges support from STScI Director's Discretionary Fund. K.F. acknowledges support through the ESA research fellowship. K.B. acknowledges support through Mini Grant INAF 2022 TRAME@JWST (TRacing the Accretion Metallicity rELationship with NIRSpec@JWST). O.C.J. acknowledges support from an STFC Webb fellowship. C.N. acknowledges the support of an STFC studentship (2645535). M.M., N.H., and L.L. acknowledge that a portion of their research was carried

out at the Jet Propulsion Laboratory, California Institute of Technology, under a contract with the National Aeronautics and Space Administration (80NM0018D0004). A.S.H. is supported in part by an STScI Postdoctoral Fellowship. We thank Brunella Nisini, Teresa Giannini, Juan Alcalá, and Manuele Gangi for their discussions.

Facility: JWST (NIRSpec, NIRCам).

Software: eMPT (N. Bonaventura et al. 2023), NIPS (C. Alves de Oliveira et al. 2018b).

Appendix

Accretion Luminosity and Mass Accretion Rate

We derived the accretion luminosities listed in Table 1 following the relationships of J. M. Alcalá et al. (2017) between accretion luminosity and line luminosity of the type $\log(L_{\text{acc}}/L_{\odot}) = a \times \log(L_{\text{line}}/L_{\odot}) + b$, where a and b are specific to each line and L_{line} is the line luminosity corrected for extinction. The values of $L(\text{Br}\gamma)$ are those measured in this work, while those of $L(\text{H}\alpha)$ are taken from G. De Marchi et al. (2011a). The coefficients (and their uncertainties) are $a = 1.13$ (0.05) and $b = 1.74$ (0.19) for $\text{H}\alpha$, and $a = 1.19$ (0.10) and $b = 4.02$ (0.51) for $\text{Br}\gamma$.

The extinction correction at the wavelength of $\text{Br}\gamma$ was computed from the A_V values measured by G. De Marchi et al. (2011a) for each star (see Table 1) and converted to the K band by adopting the standard relationship (H. C. van de Hulst 1949; G. H. Rieke & M. J. Lebofsky 1985) $A_K \simeq 0.1 A_V$. The typical reddening is $A_K = 0.05 \pm 0.01$ and after extinction correction $L(\text{Br}\gamma)$ becomes about 5% brighter. Although the effect introduced by extinction is comparable to the typical calibration uncertainty, it is systematic and we corrected for it.

The mass accretion rates (Table 1) were computed from the freefall equation

$$L_{\text{acc}} \simeq \frac{G M_* \dot{M}_{\text{acc}}}{R_*} \left(1 - \frac{R_*}{R_{\text{in}}} \right), \quad (\text{A1})$$

where G is the gravitational constant, M_* and R_* the mass and photospheric radius of the star, and R_{in} the inner radius of the accretion disk, from where the accretion flow is supposed to start. The values of M_* and R_* (listed in Table 1) are from G. De Marchi et al. (2011a). The value of R_{in} depends on how exactly the accretion disk is coupled with the magnetic field of the star and is therefore uncertain. Following E. Gullbring et al. (1998), we adopt $R_{\text{in}} = 5 R_*$ for all PMS objects.

Concerning the uncertainties, besides those on the accretion luminosity, those on the R_*/M_* ratio also contribute to the uncertainty on \dot{M}_{acc} . The uncertainty on R_*/M_* is dominated by the reddening correction (G. De Marchi et al. 2010). Given the typical $A_V = 0.5$ extinction of our sources, adopting a conservative 0.1 mag uncertainty on A_V results in an uncertainty of $\sim 3\%$ on R_*/M_* . This is smaller than the systematic uncertainty on the mass alone, which G. De Marchi et al. (2010) estimate to be about 20% because the effects of the extinction on R_* and M_* are correlated. Therefore, the 0.25 dex uncertainty on the $L(\text{line}) - L_{\text{acc}}$ conversion dominates the uncertainty on \dot{M}_{acc} . The overall cumulative relative uncertainty on the mass accretion rate is estimated to be ~ 0.42 dex (J. M. Alcalá et al. 2017).

ORCID iDs

Guido De Marchi  <https://orcid.org/0000-0001-7906-3829>
 Giovanna Giardino  <https://orcid.org/0000-0002-9262-7155>
 Katia Biazzo  <https://orcid.org/0000-0002-1892-2180>
 Nino Panagia  <https://orcid.org/0000-0002-9309-9737>
 Elena Sabbi  <https://orcid.org/0000-0003-2954-7643>
 Tracy L. Beck  <https://orcid.org/0000-0002-6881-0574>
 Massimo Robberto  <https://orcid.org/0000-0002-9573-3199>
 Peter Zeidler  <https://orcid.org/0000-0002-6091-7924>
 Olivia C. Jones  <https://orcid.org/0000-0003-4870-5547>
 Margaret Meixner  <https://orcid.org/0000-0002-0522-3743>
 Katja Fahrion  <https://orcid.org/0000-0003-2902-8608>
 Nolan Habel  <https://orcid.org/0000-0002-2667-1676>
 Conor Nally  <https://orcid.org/0000-0002-7512-1662>
 Alec S. Hirschauer  <https://orcid.org/0000-0002-2954-8622>
 David R. Soderblom  <https://orcid.org/0000-0002-0322-8161>
 Omnarayani Nayak  <https://orcid.org/0000-0001-6576-6339>
 Laura Lenkić  <https://orcid.org/0000-0003-4023-8657>
 Ciaran Rogers  <https://orcid.org/0000-0001-5742-2261>
 Bernhard Brandl  <https://orcid.org/0000-0001-9737-169X>
 Charles D. Keyes  <https://orcid.org/0000-0002-4834-369X>

References

- Alcalá, J. M., Gangi, M., Biazzo, K., et al. 2021, *A&A*, **652**, A72
 Alcalá, J. M., Manara, C., Natta, A., et al. 2017, *A&A*, **600**, A20
 Alcalá, J. M., Natta, A., Manara, C., et al. 2014, *A&A*, **561**, A2
 Alves de Oliveira, C., Birkmann, S., Böker, T., et al. 2018a, *Proc. SPIE*, **10704**, 107040Q
 Alves de Oliveira, C., Luetzgendorf, N., Ferruit, P., et al. 2018b, The NIRSpec Instrument Pipeline Software, NIPS, <https://jwst-tools.cosmos.esa.int>
 Armitage, P. J. 2010, in Handbook of Exoplanets, ed. H. Deeg & J. Belmonte (Berlin: Springer), **135**
 Baker, J. G., & Menzel, D. H. 1938, *ApJ*, **88**, 52
 Baraffe, I., & Chabrier, G. 2010, *A&A*, **521**, A44
 Baraffe, I., Chabrier, G., & Gallardo, J. 2009, *ApJL*, **702**, L27
 Baraffe, I., Elbakyan, V. G., Vorobyov, E. I., et al. 2017, *A&A*, **597**, A19
 Bessell, M. S., Castelli, F., & Plez, B. 1998, *A&A*, **333**, 231
 Biazzo, K., Alcalá, J., Covino, E., et al. 2012, *A&A*, **542**, 115
 Biazzo, K., Beccari, G., Marchi, G. D., & Panagia, N. 2019, *ApJ*, **875**, 51
 Birkmann, S. M., Giardano, G., Sirianni, M., et al. 2022, *Proc. SPIE*, **12180**, 121802P
 Bonaventura, N., Jakobsen, P., Ferruit, P., et al. 2023, *A&A*, **672**, A40
 Bressan, A., Marigo, P., Girardi, L., et al. 2012, *MNRAS*, **427**, 127
 Cardelli, J. A., Clayton, G. C., & Mathis, J. S. 1989, *ApJ*, **345**, 245
 Carini, R., Biazzo, K., De Marchi, G., et al. 2022, *A&A*, **663**, A74
 Castelli, F., & Kurucz, R. L. 2003, in IAU Symp. 210, Modelling of Stellar Atmospheres, ed. N. Piskunov, W.W. Weiss, & D.F. Gray (San Francisco, CA: ASP), **A20**
 Cusano, F., Ripepi, V., Alcalá, J., et al. 2011, *MNRAS*, **410**, 227
 De Marchi, G., Beccari, G., & Panagia, N. 2013, *ApJ*, **775**, 68
 De Marchi, G., & Panagia, N. 2014, *MNRAS*, **445**, 93
 De Marchi, G., Panagia, N., & Romaniello, M. 2010, *ApJ*, **715**, 1
 De Marchi, G., Panagia, N., Romaniello, M., Sabbi, E., Sirianni, M., et al. 2011a, *ApJ*, **740**, 11
 De Marchi, G., Panagia, N., & Sabbi, E. 2011b, *ApJ*, **740**, 10
 De Marchi, G., Panagia, N., Sabbi, E., et al. 2016, *MNRAS*, **455**, 4373
 De Marchi, G., Panagia, N., & Beccari, G. 2017, *ApJ*, **846**, 110
 Degl'Innocenti, S., Prada Moroni, P., Marconi, M., et al. 2008, *Ap&SS*, **316**, 25
 Dotter, A. 2016, *ApJS*, **222**, 8
 Ercolano, B., Clarke, C. J., & Drake, J. J. 2009, *ApJ*, **699**, 1639
 Ercolano, B., Drake, J. J., Raymond, J. C., & Clarke, C. C. 2008, *ApJ*, **688**, 398
 Fahrion, K., & De Marchi, G. 2023, *A&A*, **671**, L14
 Fedele, D., van den Ancker, M. E., Henning, T., et al. 2010, *A&A*, **510**, A72
 Ferruit, P., Jakobsen, P., Giardino, G., et al. 2022, *A&A*, **661**, A81
 Fitzpatrick, E. 1999, *PASP*, **111**, 63
 Frasca, A., Biazzo, K., Alcalá, J., et al. 2017, *A&A*, **602**, A33
 Fynbo, J., Starling, R., Ledoux, C., et al. 2006, *ApJ*, **451**, L47
 Gahm, G. F., Walter, F. M., Stempels, H. C., et al. 2008, *A&A*, **482**, L35
 Gangi, M., Antonucci, S., Biazzo, K., et al. 2022, *A&A*, **667**, A124
 Gardiner, L. T., & Hawkins, M. R. S. 1991, *MNRAS*, **251**, 174

- Garufi, A., Benisty, M., Pinilla, P., et al. 2018, *A&A*, **620**, A94
- Gredel, R., & Dalgarno, A. 1995, *ApJ*, **446**, 852
- Greene, T. P., Barsony, M., & Weintraub, D. A. 2010, *ApJ*, **725**, 1100
- Guarcello, M. G., Biazzo, K., Drake, J., et al. 2021, *A&A*, **650**, A157
- Gullbring, E., Hartmann, L., Briceño, C., & Calvet, N. 1998, *ApJ*, **492**, 323
- Gustafsson, B., Edvardsson, B., Eriksson, K., et al. 2008, *A&A*, **486**, 951
- Habel, N., Nally, C., Lenkić, L., et al. 2024, *ApJ*, **971**, 108
- Haisch, K. E., Lada, E. A., & Lada, C. J. 2001, *ApJ*, **553**, 153
- Hartmann, L., Herczeg, G., & Calvet, N. 2016, *ARA&A*, **54**, 135
- Hauschildt, P. H., Allard, F., & Baron, E. 1999, *ApJ*, **512**, 377
- Hayashi, C. 1966, *ARA&A*, **4**, 171
- Hennekemper, E., Gouliermis, D. A., Henning, T., Brandner, W., & Dolphin, A. E. 2008, *ApJ*, **672**, 914
- Herczeg, G. J., Cruz, K. L., & Hillenbrand, L. A. 2009, *ApJ*, **696**, 1589
- Herczeg, G. J., & Hillenbrand, L. A. 2014, *ApJ*, **786**, 97
- Hernandez, J., Hartmann, L., Calvet, N., et al. 2008, *ApJ*, **686**, 1195
- Hilditch, R. W., Howarth, I. D., & Harries, T. J. 2005, *MNRAS*, **357**, 304
- Johnson, J. L., & Li, H. 2012, *ApJ*, **751**, 81
- Jones, O. C., Nally, C., Habel, N., et al. 2023, *NatAst*, **7**, 694
- Keller, S. C., & Wood, P. R. 2006, *ApJ*, **642**, 834
- Kuffmeier, M., Frimann, S., Jensen, S. S., & Haugbølle, T. 2018, *MNRAS*, **475**, 2642
- Kupka, F., Dubernet, M.-L., & VAMDC Collaboration 2011, *BaltA*, **20**, 503
- Larson, R. B. 2003, *RPPH*, **66**, 1651
- Lilly, S., Le Fevre, O., Hammer, F., et al. 1996, *ApJL*, **460**, L1
- Madau, P., Ferguson, H. C., Dickinson, M. E., et al. 1996, *MNRAS*, **283**, 1388
- Maiz Apellaniz, J., Evans, C., Barba, R., et al. 2014, *A&A*, **564**, A63
- Mamajek, E. E. 2009, in AIP Conf. Proc. 1158, *Exoplanets and Disks: their Formation and Diversity*, ed. T. Usuda, I. Miki, & T. Motohide (Melville, NY: AIP), **3**
- Martin, S. C. 1996, *ApJ*, **470**, 537
- Montes, D., Fernandez-Figueroa, M. J., De Castro, E., et al. 1995, *A&A*, **294**, 165
- Murray, C. E., Hasselquist, S., Peek, J. E. G., et al. 2024, *ApJ*, **962**, 120
- Muzerolle, J., Calvet, N., & Hartmann, L. 1998, *ApJ*, **492**, 743
- Muzerolle, J., Calvet, N., & Hartmann, L. 2001, *ApJ*, **550**, 944
- Najita, J. R., & Bergin, E. A. 2018, *ApJ*, **864**, 168
- Nidever, D., Majewski, S., Muñoz, R., et al. 2011, *ApJL*, **733**, L10
- Niedzielski, A., Goździewski, K., Wolszczan, A., et al. 2009, *ApJ*, **693**, 276
- Palla, F., & Stahler, S. W. 1999, *ApJ*, **525**, 772
- Pfalzner, S., Dehghani, S., & Michel, A. 2022, *ApJL*, **939**, L10
- Ramirez-Tannus, M. C., Bik, A., Cuijpers, L., et al. 2023, *ApJL*, **958**, L30
- Richert, A. J. W., Getman, K. V., Feigelson, E. D., et al. 2018, *MNRAS*, **477**, 5191
- Rieke, G. H., & Lebofsky, M. J. 1985, *ApJ*, **288**, 618
- Rogers, C., De Marchi, G., & Brandl, B. 2024, *A&A*, **684**, L8
- Sabbi, E., Sirianni, M., Nota, A., et al. 2007, *AJ*, **133**, 44
- Sabbi, E., Zeidler, P., van der Marel, R. P., et al. 2022, *ApJ*, **936**, 135
- Setiawan, J., Klement, R. J., Henning, T., et al. 2010, *Sci*, **330**, 1642
- Shu, F. H., Adams, F. C., & Lizano, S. 1987, *ARA&A*, **25**, 23
- Siess, L., Dufour, E., & Forestini, M. 2000, *A&A*, **358**, 593
- Sigurdsson, S., Richer, H. B., Hansen, B. M., Stairs, I. H., & Thorsett, S. E. 2003, *Sci*, **301**, 193
- Snedden, C., Bean, J., Ivans, I., et al., 2012 MOOG: LTE line analysis and spectrum synthesis, Astrophysics Source Code Library, ascl:[1202.009](#)
- Stoeck, F., White, R., Smith, M., et al. 2008, in ASP Conf. Ser. 394, *Astronomical Data Analysis Software and Systems XVII*, ed. R. Argyle, P. Bunclark, & J. Lewis (San Francisco, CA: ASP), **505**
- Storey, P. J., & Hummer, D. G. 1995, *MNRAS*, **272**, 41
- STScI Development Team, 2020 stsynphot: synphot for HST and JWST, Astrophysics Source Code Library, ascl:[2010.003](#)
- Tang, J., Bressan, A., Rosenfield, P., et al. 2014, *MNRAS*, **445**, 4287
- Tognelli, E., Prada Moroni, P. G., & Degl'Innocenti, S. 2011, *A&A*, **533**, A109
- Tsilia, S., De Marchi, G., & Panagia, N. 2023, *A&A*, **675**, A203
- Valenti, J., & Piskunov, N. 1996, *A&AS*, **118**, 595
- van de Hulst, H. C. 1949, *RAOU*, **11**, 2
- Venuti, L., Bouvier, J., Flaccomio, E., et al. 2014, *A&A*, **570**, A82
- Vlasblom, M., & De Marchi, G. 2023, *A&A*, **675**, A204
- Vorobyov, E. I., Baraffe, I., Harries, T., et al. 2013, *A&A*, **557**, A35
- Yanchulova Merica-Jones, P., Sandstrom, K., Johnson, L. C., et al. 2017, *ApJ*, **847**, 102
- Yasui, C., Kobayashi, N., Tokunaga, A. T., Saito, M., & Izumi, N. 2016, *AJ*, **151**, 50
- Yasui, C., Kobayashi, N., Tokunaga, A. T., Saito, M., & Tokoku, C. 2009, *ApJ*, **705**, 54
- Yasui, C., Kobayashi, N., Tokunaga, A. T., Saito, M., & Tokoku, C. 2010, *ApJL*, **723**, L113
- Zwaan, M., van der Hulst, J., Briggs, F., et al. 2005, *MNRAS*, **364**, 1467